nature materials

Article

https://doi.org/10.1038/s41563-024-01809-z

Angle-resolved transport non-reciprocity and spontaneous symmetry breaking in twisted trilayer graphene

Received: 1 June 2023

Accepted: 16 January 2024

Published online: 22 February 2024



Check for updates

Naiyuan James Zhang 1, Jiang-Xiazi Lin 1, Dmitry V. Chichinadze 2, Yibang Wang¹, Kenji Watanabe **3**, Takashi Taniguchi **4**, Liang Fu **5**& J. I. A. Li 🏚¹⊠

The identification and characterization of spontaneous symmetry breaking is central to our understanding of strongly correlated two-dimensional materials. In this work, we utilize the angle-resolved measurements of transport non-reciprocity to investigate spontaneous symmetry breaking in twisted trilayer graphene. By analysing the angular dependence of non-reciprocity in both longitudinal and transverse channels, we are able to identify the symmetry axis associated with the underlying electronic order. We report that a hysteretic rotation in the mirror axis can be induced by thermal cycles and a large current bias, supporting the spontaneous breaking of rotational symmetry. Moreover, the onset of non-reciprocity with decreasing temperature coincides with the emergence of orbital ferromagnetism. Combined with the angular dependence of the superconducting diode effect, our findings uncover a direct link between rotational and time-reversal symmetry breaking. These symmetry requirements point towards exchange-driven instabilities in momentum space as a possible origin for transport non-reciprocity in twisted trilayer graphene.

Electronic nematicity describes the Coulomb-driven phenomenon with reduced in-plane rotational symmetry compared with the underlying crystal lattice¹⁻³. For instance, orthorhombic anisotropy emerges as the Fermi surface undergoes a quadruple distortion to save Coulomb energy. Such a Coulomb-driven phenomenon has been widely observed in a series of strongly correlated two-dimensional systems, such as strontium ruthenate, cuprate materials⁴⁻⁷ and magic-angle twisted bilayer and trilayer graphene⁸⁻¹³. Orthorhombic anisotropy features two mirror axes that are orthogonal to each other (Fig. 1a). As a result, the symmetry associated with a two-fold in-plane rotation, C_2 , is preserved. Further lifting C_2 symmetry promises to unlock a new dimension of rich physical constructions beyond orthorhombic anisotropy. It is recently proposed that an exchange interaction amongst trigonally warped Fermi pockets enables novel instabilities in momentum space. For instance, the electronic state in multilayer graphene could acquire a non-zero net momentum as charge carriers spontaneously condense into one of the Fermi pockets^{14–17}. Unlike orthorhombic anisotropy, the momentum-space instability simultaneously breaks C_2 and time-reversal symmetry T.

Rotational symmetry breaking can be identified on the basis of angle-resolved transport measurements^{4,5}, which conventionally focuses on the linear and reciprocal components of the transport response, such as the longitudinal and transverse resistances R_{\parallel} and R_{\perp} , respectively, in the limit of a small current bias. The angular dependence of R_{\parallel} and R_{\perp} is constrained by the underlying symmetry axes. A Fermi surface with quadruple distortion preserves C_2 symmetry, which gives rise to two orthogonal mirror axes (Fig. 1a, black arrows). As a function of ϕ , the longitudinal (transverse) transport response is expected

Department of Physics, Brown University, Providence, RI, USA. National High Magnetic Field Laboratory, Tallahassee, FL, USA. Research Center for Functional Materials, National Institute for Materials Science, Tsukuba, Japan. International Center for Materials Nanoarchitectonics, National Institute for Materials Science, Tsukuba, Japan. 5Department of Physics, Massachusetts Institute of Technology, Cambridge, MA, USA. 🖂 e-mail: jia_li@brown.edu

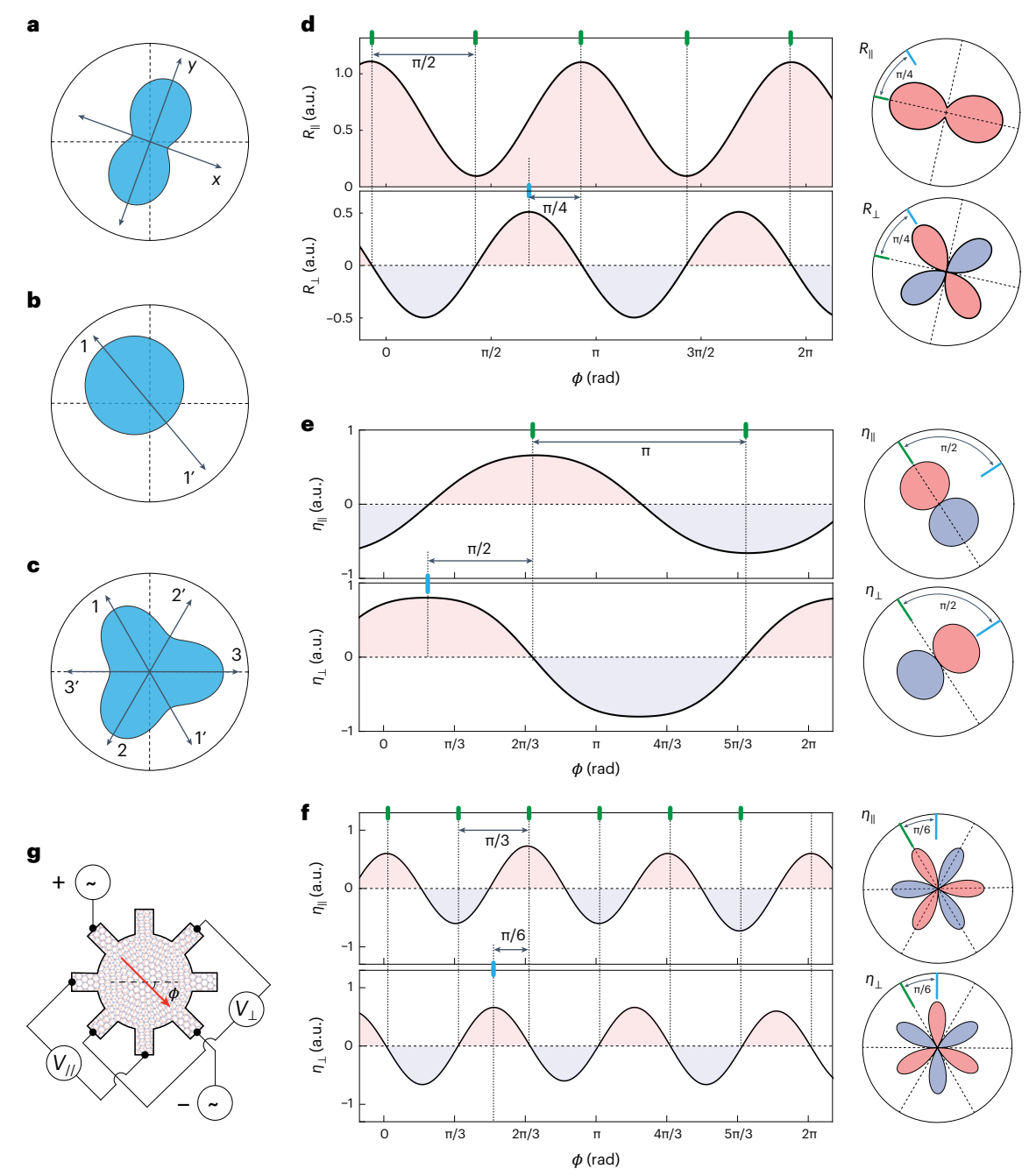


Fig. 1 | Symmetry analysis of the angle-resolved transport response. a-c, Schematic of the Fermi surface contour with different angular symmetries. The black arrows mark the azimuth direction of the mirror axis. d-f, Expected angular dependence in the transport response when the underlying electronic state is described by two (\mathbf{d}) , one (\mathbf{e}) and three (\mathbf{f}) mirror axes. The left (right) panels show the same angular dependence in the Cartesian (polar) coordinate. Panel \mathbf{d}

plots the angular dependence of longitudinal and transverse resistances R_{\parallel} and R_{\perp} , respectively, which are measured with a small d.c. current bias. Panels ${\bf e}$ and ${\bf f}$ show the angular dependence of transport non-reciprocity. ${\bf g}$, Schematic of the sunflower-shaped sample and the setup of angle-resolved measurement of transport non-reciprocity.

to be symmetric (anti-symmetric) around a mirror axis. This symmetry constraint not only gives rise to a period of π in the angular oscillation of R_{\parallel} and R_{\perp} but also accounts for a phase shift of $\pi/4$ between the longitudinal and transverse channels. Together, the angular dependence can be expressed as $R_{\parallel} = A\cos(2\phi - \alpha)$ and $R_{\perp} = A\sin(2\phi - \alpha)$. Here α defines the orientation of the mirror axes, whereas the phase shift of $\pi/4$ is captured by the cosine and sine functions.

Beyond orthorhombic anisotropy, the nature of electronic orders with C_2 symmetry breaking is directly linked to the nonlinear and non-reciprocal transport responses. For simplicity, we label

non-reciprocity in the longitudinal (transverse) channels as $\eta_{\parallel}(\eta_{\perp})$, which is simply defined as the difference in $R_{\parallel}(R_{\perp})$ between the forward-and reverse-current bias. The angular dependence of non-reciprocity shares the same symmetry constraint as the linear transport response. Consequently, $\eta_{\parallel}(\eta_{\perp})$ is expected to be maximized (zero) when current flows along the mirror line. Owing to C_2 symmetry breaking, the electronic order can have either one or three mirror axes (Fig. 1b–c). An electronic state with a single mirror axis (Fig. 1b) enables an angular period of 2π and a phase shift of $\pi/2$ between η_{\parallel} and η_{\perp} (Fig. 1e). Along the same vein, a state with three mirror axes (Fig. 1c) is identifiable by

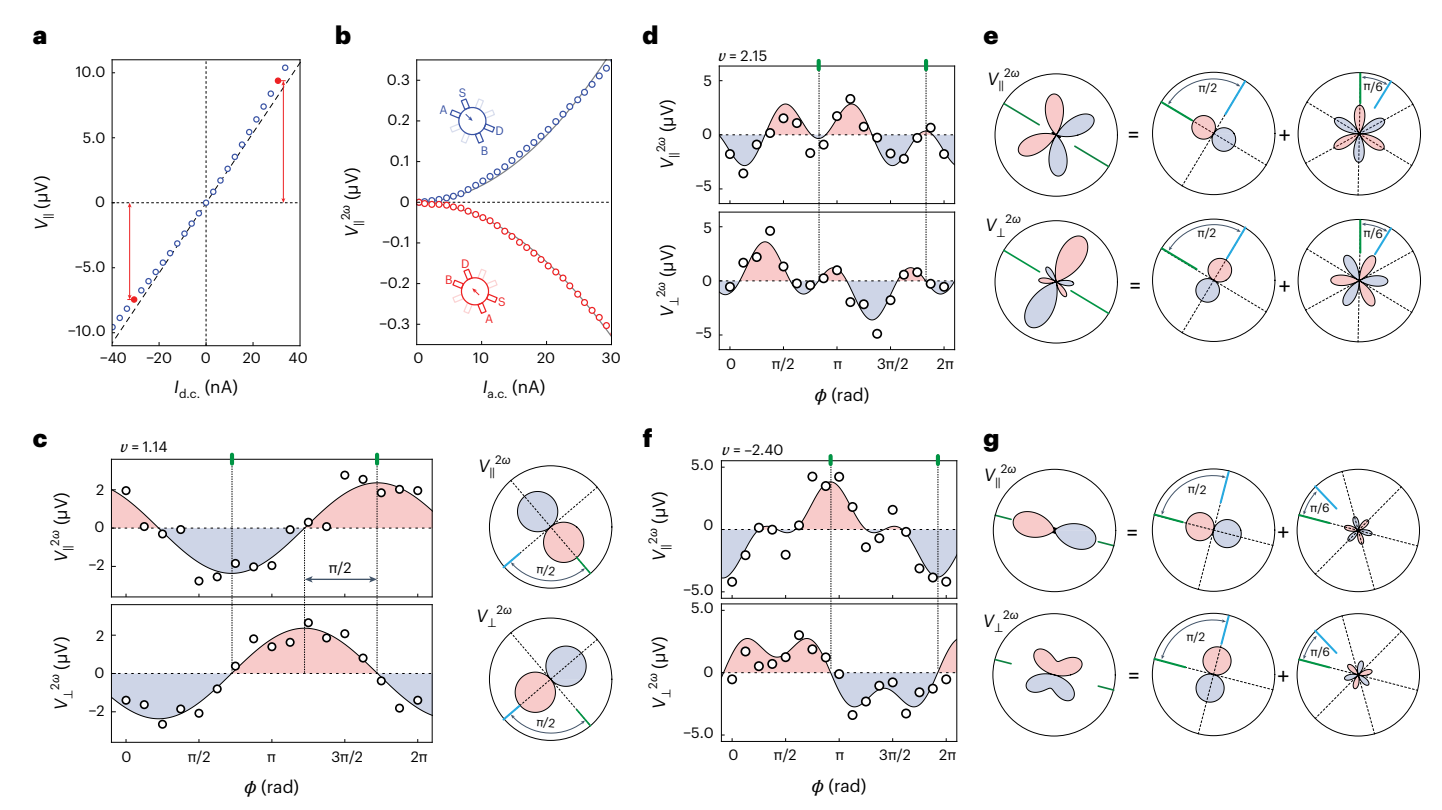


Fig. 2 | **Transport non-reciprocity in tTLG. a**, I-V characteristics measured with a d.c. current bias. The black dashed line represents the linear component of the transport response. **b**, Second-harmonic nonlinear transport response $V_{\parallel}^{2\omega}$ as a function of $I_{\rm a.c.}$, measured with current flowing along $\phi=135^\circ$ (blue) and $\phi=315^\circ$ (red). **c**, Angular dependence of $V_{\parallel}^{2\omega}$ and $V_{\perp}^{2\omega}$ measured at v=1.14. **d.e**, Angular dependence of $V_{\perp}^{2\omega}$ at v=2.15 in the Cartesian (**d**) and polar (**e**) axis. **f,g**,

Angular dependence of $V_{\parallel}^{2\omega}$ and $V_{\perp}^{2\omega}$ at v=-2.4 in the Cartesian (f) and polar (g) axis. The left panel in **e** and **g** displays the best angular fit based on equation (1), which is a linear combination of one-fold (middle) and three-fold (right) components. The green solid line marks the direction of the mirror axis. Measurements in **c**-**g** are performed at $I_{a.c.}=100$ nA. All the measurements are performed at T=20 mK and B=0.

a period of $2\pi/3$ in angular oscillation, along with a phase shift of $\pi/6$ between η_{\parallel} and η_{\perp} (Fig. 1f).

In this work, we investigate the angular dependence of transport non-reciprocity in mirror-symmetric twisted trilayer graphene (tTLG), which sheds new light on the nature of spontaneous symmetry breaking in a moiré flat band. To perform angle-resolved transport measurements. we shape tTLG samples into the sunflower geometry (Fig. 1g). By using different contact pairs as the source and drain, the sunflower geometry allows us to flow current is 16 azimuth directions in the range of $0 < \phi < 2\pi$ (Extended Data Fig. 1 shows different measurement configurations). This provides the necessary resolution to identify angular oscillations with a period of 2π and $2\pi/3$. When current flows along the azimuth direction ϕ , voltage responses $V_{\parallel}(\phi)$ and $V_{\perp}(\phi)$ are measured between the contact leads that are aligned parallel and perpendicular to the current flow direction, respectively (Fig. 1g). The longitudinal and transverse resistances are extracted as $R_{\parallel}(\phi) = V_{\parallel}(\phi)/I_{\rm d.c.}$ and $R_{\perp}(\phi) = V_{\perp}(\phi)/I_{\rm d.c.}$ whereas non-reciprocity is defined as $\eta_{\parallel}(\phi) = R_{\parallel}(\phi) - R_{\parallel}(\phi + \pi)$ and $\eta_{\perp}(\phi) = R_{\perp}(\phi) - R_{\perp}(\phi + \pi)$, respectively.

The presence of transport non-reciprocity is demonstrated by the current–voltage (I-V) characteristics (Fig. 2a), where the voltage response at large current deviates from the linear component (black dashed line). The non-reciprocity, extracted by subtracting the linear component, exhibits a quadratic current dependence (Extended Data Fig. 4). In the presence of an a.c. current bias with frequency ω , the non-reciprocal response is proportional to $\sin^2(\omega t)$, which has the same frequency modulation as $\sin(2\omega t)$. As such, η can be conveniently probed as the amplitude of the a.c. response at the second-harmonic frequency 2ω . Figure 2b plots the second-harmonic voltage response $V_{\perp}^{2\omega}$, which exhibits a quadratic dependence on the a.c. current bias. A

rotation of 180° in the measurement configuration induces a sign reversal in $V_{\parallel}^{2\omega}$. Since the sample geometry respects the rotation, the sign reversal offers a strong indication of two-fold rotational symmetry breaking. We note that non-reciprocity extracted from the d.c. I-V curve is equivalent to the second-harmonic nonlinear response (Extended Data Fig. 5).

Figure 2c–g plots the angular dependence of non-reciprocity measured at different moiré band fillings. At $\nu=1.14$, both $V_\parallel^{2\omega}$ and $V_\perp^{2\omega}$ are captured by cosine functions with a period of 2π . Figure 2c also displays a relative phase shift of $\pi/2$ across two channels. This is consistent with the presence of one mirror axis (Fig. 2c, green solid line). In comparison, the angular dependence shown in Fig. 2d,f exhibits a more complex functional form, which reveals a unique connection between the longitudinal and transverse channels. Figure 2e,g plots the polar-coordinate plot of the best angular fit for the data in Fig. 2d,f (left), which is a linear combination of the one-fold (middle) and three-fold (right) components. The green and blue solid lines in this figure mark the phases of the longitudinal and transverse channels. Between these two channels, the one-fold components display a phase shift of $\pi/2$, whereas the phases of the three-fold components are offset by $\pi/6$.

The unique connection between the longitudinal and transverse channels provides a strong constraint for identifying the functional form for the angular dependence of non-reciprocity. Both channels of non-reciprocity can be simultaneously captured by a rather simple expression:

$$\begin{split} V_{\parallel}^{2\omega}(\phi) &= V_{1}\cos(\phi - \beta) + V_{3}\cos(3(\phi - \beta)), \\ V_{\perp}^{2\omega}(\phi) &= V_{1}\sin(\phi - \beta) + V_{3}\sin(3(\phi - \beta)). \end{split} \tag{1}$$

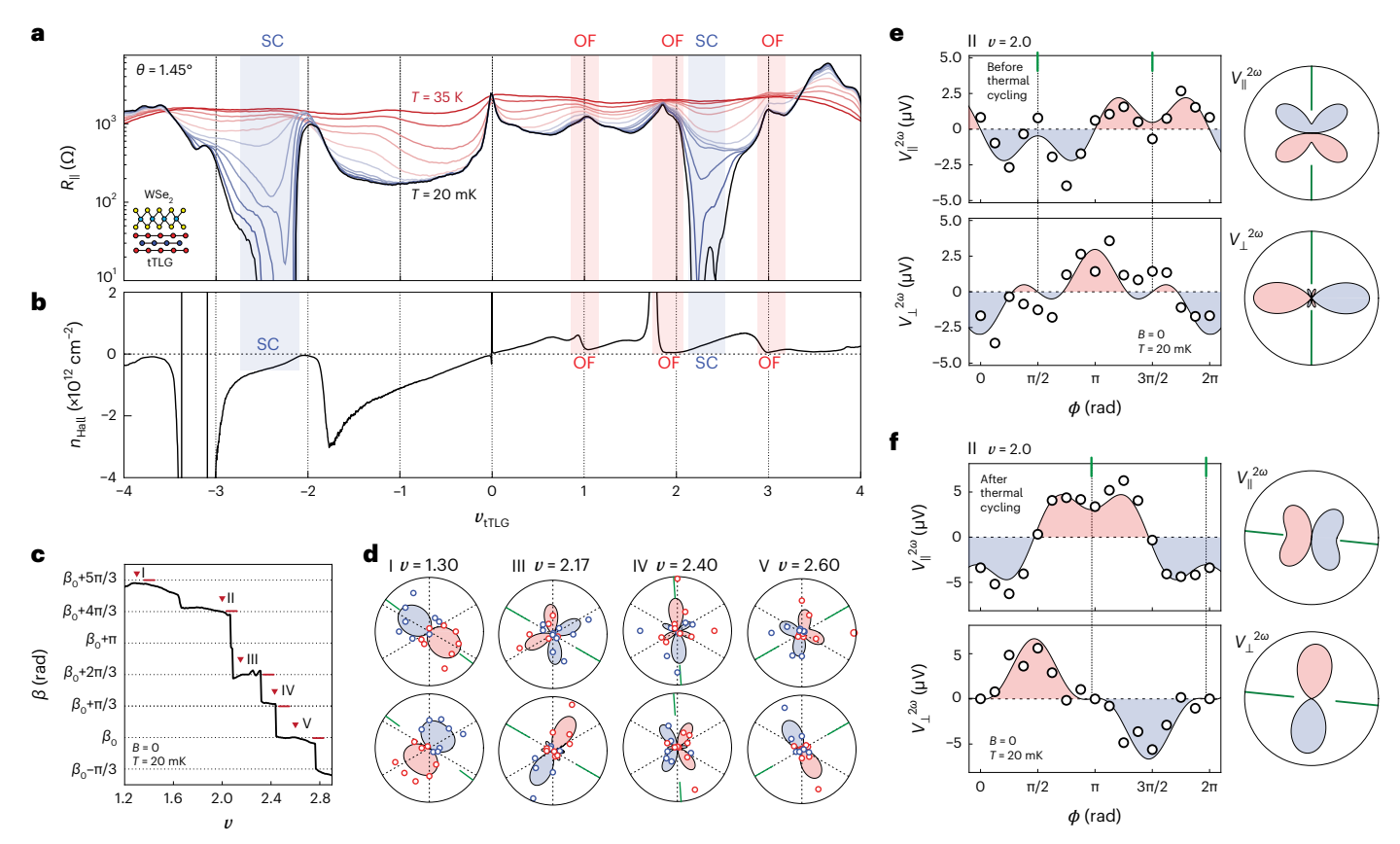


Fig. 3 | **Moiré flat band and the density dependence of non-reciprocity. a,b,** Longitudinal resistance R_{\parallel} (**a**) and Hall density $n_{\rm Hall}$ (**b**) as a function of moiré band filling ν , measured at T=20 mK and $I_{\rm d.c.}=5$ nA. The density regimes of the superconducting (SC) phase and orbital ferromagnetic (OF) order are marked with blue and red vertical stripes, respectively. The inset in **a** shows the schematic of the sample composition, where a tTLG is proximitized with a few-layer

tungsten diselenide (WSe₂) crystal. **c**, Mirror-axis orientation β as a function of moiré band filling. **d**, Polar-coordinate plots of the angular dependence of transport non-reciprocity measured from plateaus I, III, IV and V in **a**. **e**,**f**, Angular dependence of $V_{\parallel}^{2\omega}$ and $V_{\perp}^{2\omega}$ measured at v=2.0, which is on plateau II before (**e**) and after (**f**) a thermal cycle. Measurements in **c**-**f** are performed at T=20 mK, B=0 and $I_{a.c.}=100$ nA.

Here β defines the azimuth orientation of the mirror axis. Also, $V_1(V_3)$ denotes the amplitude of the one-fold (three-fold) component of the angular oscillation, whereas the phase shift between the longitudinal and transverse channels is naturally captured by the cosine and sine functions. Equation (1) resembles a Fourier expansion around a mirror axis, where the longitudinal (transverse) non-reciprocity is expressed by the linear combination of $\cos(N\phi)$ ($\sin(N\phi)$). Although an expansion allows any odd integer values of N, only N=1 and 3 are observed in our measurement. Extended Data Fig. 9 shows non-reciprocity measured with a higher angular resolution, which confirms the dominating role of the N=1 and 3 components.

The quality of the angular fit can be gauged on the basis of the relative root mean squared error (RRMSE) (Extended Data Figs. 6 and 7). RRMSE exhibits sharp minima around the optimal fitting parameter, suggesting that V_1 , V_3 and β are uniquely determined. RRMSE of the best fit is around 0.05 for the angular dependence shown in Fig. 2. This is a strong indication that equation (1) offers a good description for the angular dependence of non-reciprocity. The sunflower geometry also enables measurement and analysis schemes beyond the simple angle-resolved transport. These schemes offer direct assessment for the uniformity of the sample. Theoretically, the potential distribution across the circumference of the sample is solely determined by the conductivity matrix¹⁸. This distribution can be mapped through the linear transport response from an extensive series of measurement configurations (Extended Data Fig. 8)¹³. By fitting the potential distribution, a single conductivity matrix is extracted with an RRMSE of 0.017.

The excellent fit quality points towards a uniform transport response across the entire sample, which indicates that the impact from moiré disorder and inhomogeneity is negligible.

Next, we will examine the linear transport response of tTLG. As shown in Fig. 3a,b, the tTLG sample exhibits a series of hallmark signatures of a moiré flat band. For instance, resistance peaks in R_{\parallel} are observed near $\nu_{\rm tTLG}$ = -2, +1, +2 and +3 (Fig. 3a), which coincides with resets in the Hall density n_{Hall} (Fig. 3b). This is consistent with previous observations from magic-angle twisted bilayer and trilayer graphene, where valley and spin degeneracies are spontaneously lifted near integer band filling, giving rise to a cascade of Fermi surface reconstructions¹⁹⁻²³. As shown in Fig. 3a (inset), the tTLG is proximitized with a WSe₂ crystal. Supplementary Fig. 7 investigates the influence of the proximity effect through a comparison with another tTLG sample without the WSe₂ crystal. In both samples, Fermi surface reconstruction, evidenced by the resistance peak and Hall density reset, occurs at the same band fillings. Superconductivity in both samples emerges near half-filling of electron- and hole-doped bands. Moreover, the band filling-temperature (v-T) maps from both samples reveal the same resistance oscillation at high temperature. Combined, these observations suggest that the nature of isospin degeneracy lifting is unaffected by the proximity effect. The orbital ferromagnetic order, however, is only observed in the tTLG sample with the proximity effect. This is consistent with previous observations of proximity-induced anomalous Hall effect in magic-angle twisted bilayer graphene²⁴.

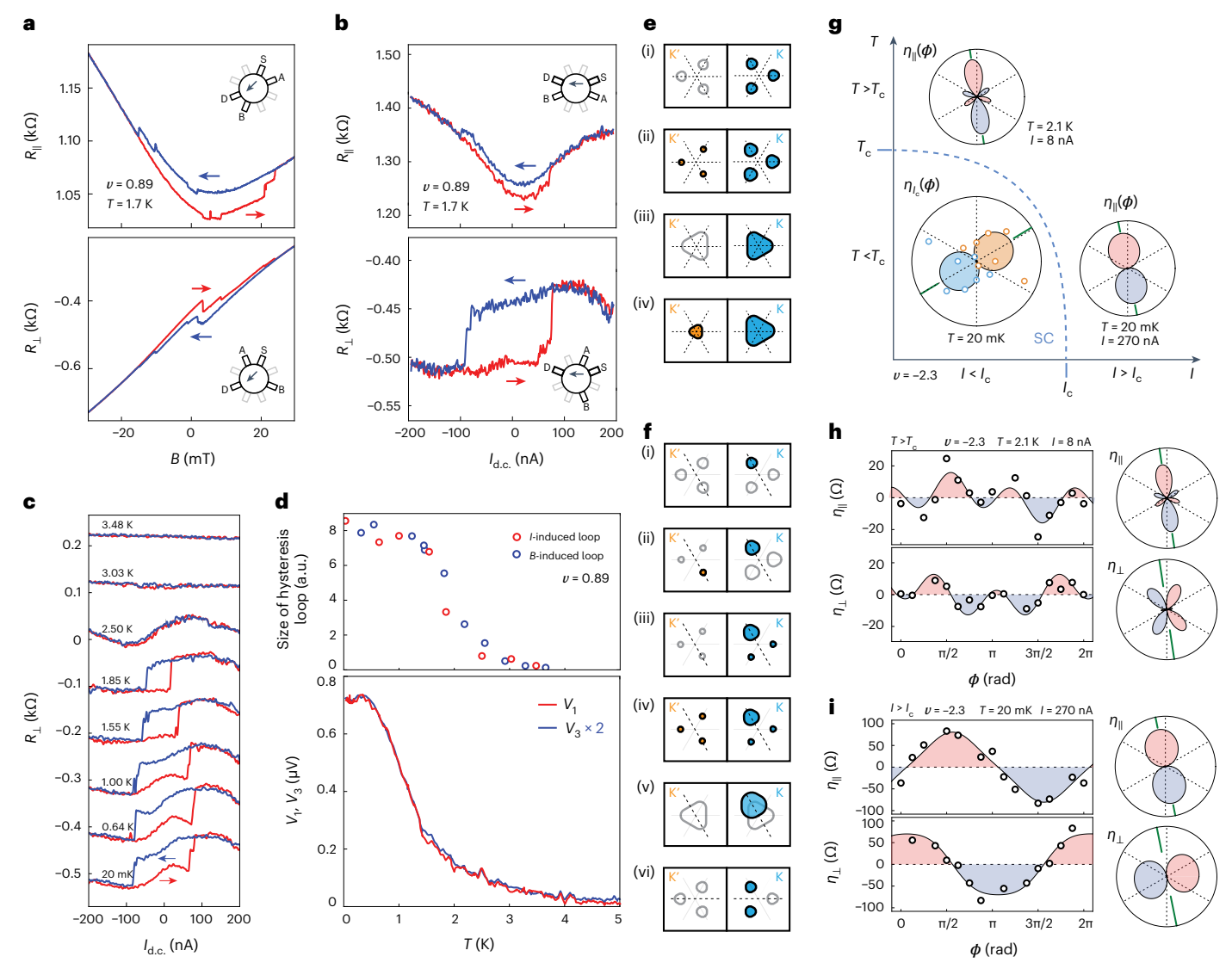


Fig. 4 | **Non-reciprocity, orbital ferromagnetism and superconductivity. a,b,** Hysteretic transitions at v = 0.89 are induced by sweeping magnetic field B (**a**) and d.c. current bias $I_{\rm d.c.}(\mathbf{b})$ back and forth. The top and bottom panels show the longitudinal and transverse resistances R_{\parallel} and R_{\perp} , respectively. **c,** Current-induced hysteresis loops measured at different temperatures. **d,** Size of the hysteresis loops (top) is compared with the temperature dependence of V_1 and V_3 (bottom), which are extracted from the angular oscillation in $V_{\parallel}^{2\omega}$ and $V_{\perp}^{2\omega}$ according to equation (1). **e,f,** Schematic of the Fermi surface occupation across valley K and K' in the presence of valley polarization with three mirror axes (**e**) and

momentum polarization with one mirror axis (**f**). The spin degree of freedom is omitted. **g**, Schematic of the current–temperature (I–I) phase diagram at the optimal doping of the superconducting phase. The blue dashed line marks the SC–normal state transition. The angular dependence of non-reciprocity is shown for the superconducting ($\eta_{\rm lc}(\phi)$) and normal phases ($\eta_{\parallel}(\phi)$). Supplementary Fig. 13 provides more details on the non-reciprocity in superconducting transport. **h,i**, Angular dependence of non-reciprocity ($\eta_{\parallel}({\rm top})$ and $\eta_{\perp}({\rm bottom})$), measured in the normal state at $T > T_{\rm c}({\bf h})$ and $I > I_{\rm c}({\bf i})$. Measurements are performed at the optimal density of the superconducting phase, that is, v = -2.3.

Beyond the sequence of Fermi surface reconstructions, angle-resolved non-reciprocity measurement reveals a new type of cascade phenomenon. Figure 3c,d shows the angular dependence of $V_{\perp}^{2\omega}$ and $V_{\perp}^{2\omega}$ in the density regime of $1.2 < v_{\rm tTLG} < 2.8$. The orientation of the mirror axis, marked by the green solid line in this figure, is determined by the best angular fit based on equation (1). As a function of band filling, β exhibits a series of plateaus (Fig. 3c, black solid line), which point towards a cascade of rotations in the mirror axis. The values of β between adjacent plateaus, marked as I through V, are offset by integer multiples of $\pi/3$. This defines six characteristic directions, highlighting a possible link to the crystallographic axes of the underlying moiré lattice.

According to the angular dependence of non-reciprocity (Fig. 3d), the underlying electronic order features a single mirror axis, which is indicative of broken three-fold rotational symmetry C_3 . The fact that the mirror axis rotates with varying moiré band fillings stipulates that

 C_3 breaking cannot be accounted for by the influence of hetero-strain alone. In addition, we show that a hysteretic rotation in the mirror axis can be induced by thermally cycling the sample or the application of a large current bias. Figure 3e, f compares the angular dependence of non-reciprocity measured at the same moiré filling from two consecutive cool-down cycles. The best angular fit with equation (1) reveals a prominent rotation in the mirror axis before (Fig. 3e) and after (Fig. 3f) the thermal cycle. Similarly, the application of a large current bias also enables a prominent rotation in the mirror axis (Extended Data Fig. 2b). Such hysteretic transition is associated with a hysteresis loop in the second-harmonic nonlinear response as the current bias is swept back and forth (Extended Data Fig. 2c). These hysteretic transitions point towards nearly degenerate electronic orders with different mirror-axis orientations. The degeneracy is lifted by the process of spontaneous rotational symmetry breaking.

The foremost question is the microscopic origin underlying the rotational symmetry breaking. To address this question, we first consider the requirements of C_2 symmetry breaking in association with time-reversal symmetry T. There are two possible scenarios (Supplementary Information provides a detailed discussion): (1) C_2 is broken and T is preserved. This scenario can be enabled by Berry curvature dipole and skew scattering $^{25-28}$; (2) C_2 and T breaking occur simultaneously. Owing to the influence of trigonal warping in tTLG 29,30 , C_2 and T breaking are naturally realized by the presence of valley polarization, which describes an imbalanced charge carrier occupation of the Fermi surface across different corners of the Brillouin zone $^{31-35}$. In the presence of sublattice polarization, valley polarization is directly linked to an orbital ferromagnetic order, which is identifiable through the hysteretic transitions of the anomalous Hall effect 24,36,37 .

Given the hysteretic rotation in the mirror axis and the evolution with moiré band filling, the angular dependence of non-reciprocity probably cannot be accounted for by the Berry curvature dipole or skew scattering. Therefore, we examine the potential role of valley polarization and orbital ferromagnetism. In the tTLG sample, orbital ferromagnetic order is observed near integer fillings of the electron-doped band. Figure 4a,b plots the transport response measured at v = 0.89as a function of magnetic field B and d.c. current bias $I_{d.c.}$ As B and $I_{d.c.}$ are swept back and forth, hysteretic transitions are observed in both R_{\parallel} (top) and R_{\perp} (bottom) in this figure. This is in excellent agreement with the anomalous Hall effect observed in other multilayer graphene heterostructures^{24,37-39}. Owing to the presence of a Dirac-like band, the tTLG sample is always metallic, even when the moiré flat band develops an energy gap with the emergence of orbital ferromagnetism. The metallic sample gives rise to a B-dependent background in the Hall resistance, making it challenging to observe the magnetic hysteresis loop. However, the *I*-induced hysteresis is clearly detectable in both R_{\parallel} and R_{\perp} , since the Hall resistance background is unaffected by the current bias. Both magnetic and current-induced hysteresis exhibit a sharp onset with decreasing temperature (Fig. 4c and Supplementary Fig. 12), which defines the emergence of the orbital ferromagnetic order.

The area of the hysteresis loop, A_{\perp}^B and A_{\perp}^I , offers a gauge for the strength of the orbital ferromagnetic order. With decreasing temperature, the sharp onset in A_{\perp}^B and A_{\perp}^I (Fig. 4d, top) coincides with the onset of transport non-reciprocity, which is shown as the temperature dependence of V_1 and V_3 (Fig. 4d, bottom), extracted from the angular oscillation of non-reciprocity. The temperature dependence points towards a direct link between transport non-reciprocity, valley polarization and orbital ferromagnetism.

It should be noted that valley polarization breaks C_2 and T, but it preserves their product, namely, C_2T . Since the realization of an orbital ferromagnetic order requires C_2T breaking, valley polarization in tTLG is distinct from orbital ferromagnetism. We propose that C_2T breaking is not a necessary ingredient for transport non-reciprocity. This is further supported by the fact that non-reciprocity is universally observed across the moiré band (Supplementary Fig. 14), even in the absence of the anomalous Hall effect. The strength of non-reciprocity, reflected by the angular oscillation amplitude V_1 , exhibits density modulation with the cascade of Fermi surface reconstructions (Supplementary Fig. 14a). This highlights the direct link between non-reciprocity and a valley-imbalanced charge carrier occupation.

Figure 4e shows the schematic of valley-imbalanced Fermi surface occupation, which includes scenarios with three Fermi pockets (panels (i) and (ii)) or one large Fermi surface per valley (panels (iii) and (iv)). A valley imbalance could also arise from a partial polarization, where carriers occupy both valleys (panels (ii) and (iv)). Regardless of the details, a valley-imbalanced Fermi surface occupation has three mirror axes (Fig. 4e, black dashed lines). The angular dependence of non-reciprocity with non-zero V_1 , therefore, requires an additional ingredient of C_3 symmetry breaking. This symmetry requirement is naturally satisfied by the exchange-driven instability in momentum

space, which breaks C_3 by inducing charge carrier condensation into a subset of Fermi pockets. Figure 4f shows a series of Fermi surface occupations with one mirror axis (black dashed line). Panel (i) displays a state with full momentum polarization, where all the carriers condense into one Fermi pocket. Further, panel (iv) represents a partial momentum polarization, with one Fermi pocket being slightly larger compared with the other five. It should be noted that non-reciprocity diminishes for a valley-balanced carrier occupation. This allows valley and momentum polarizations to be detected through non-reciprocity with high sensitivity. As a result, the observed non-reciprocity could arise from an extremely subtle imbalance in carrier occupation across Fermi pockets and valleys. This allows the momentum-space instability to emerge as a perturbation to other types of electronic order, such as orthorhombic anisotropy, and still accounts for the observed angular dependence in non-reciprocity.

Next, we discuss the potential influence of certain scattering mechanisms, such as skew scattering and Berry curvature dipole $^{25-28}$. Apart from hysteretic rotation in the mirror axis, we note that non-reciprocity in tTLG is observed only at T < 5 K (Fig. 4d and Supplementary Fig. 15), which is much lower compared with the typical onset temperature of scattering around hundreds of kelvins $^{25-28}$. Nevertheless, the presence of scattering could indirectly influence transport non-reciprocity. The exact role of scattering will certainly attract future efforts aiming to better understand the microscopic origin of transport non-reciprocity.

Despite the lack of a microscopic understanding, it is instructive to examine the phenomenological behaviour of the superconducting diode effect. Non-reciprocity in superconducting transport is defined as an inequality in the critical supercurrent between forward- and reverse-current bias: $\eta_{I_c}(\phi) = I_c(\phi) - I_c(\phi + \pi)$ (refs. 41,42). To minimize the potential influence of the normal state at large current, we operationally define the critical current I_c as the current bias where the measured differential resistance becomes larger than the noise floor (Supplementary Fig. 13, vertical arrows). At the optimal density of the superconducting phase, the angular dependence of η_{I_c} (Fig. 4g, bottom-left inset) is best fit by a cosine function with a period of 2π . This defines a single mirror axis, which indicates C_3 symmetry breaking.

Figure 4h–i plots the angular dependence of non-reciprocity measured from the normal state at $T > T_c$ (Fig. 4h) and $I > I_c$ (Fig. 4i). The angular dependence points towards a single mirror axis that simultaneously breaks C_2 and C_3 symmetries. The similarity between the normal and superconducting phases raises the possibility that superconductivity inherits the broken symmetries of the normal state. Since the superconducting diode effect requires broken time-reversal symmetry T, transport non-reciprocity in the superconducting and normal phases suggests that C_2 , C_3 and T are simultaneously broken, which is consistent with symmetry requirements of the momentum-space instability.

In summary, the angle-resolved measurement of transport non-reciprocity offers an effective tool to identify broken symmetries that describe the electronic order in mirror-symmetric tTLG. The angular dependence of transport non-reciprocity reveals a symmetry axis, which points towards the momentum-space instability as a possible mechanistic explanation for the zero-field superconducting diode effect⁴¹.

Online content

Any methods, additional references, Nature Portfolio reporting summaries, source data, extended data, supplementary information, acknowledgements, peer review information; details of author contributions and competing interests; and statements of data and code availability are available at https://doi.org/10.1038/s41563-024-01809-z.

References

 Fradkin, E., Kivelson, S. A., Lawler, M. J., Eisenstein, J. P. & Mackenzie, A. P. Nematic Fermi fluids in condensed matter physics. *Annu. Rev. Condens. Matter Phys.* 1, 153–178 (2010).

- Oganesyan, V., Kivelson, S. A. & Fradkin, E. Quantum theory of a nematic Fermi fluid. Phys. Rev. B 64, 195109 (2001).
- Kivelson, S. A., Fradkin, E. & Emery, V. J. Electronic liquid-crystal phases of a doped Mott insulator. *Nature* 393, 550–553 (1998).
- Wu, J., Bollinger, A., He, X. & Božović, I. Spontaneous breaking of rotational symmetry in copper oxide superconductors. *Nature* 547, 432–435 (2017).
- 5. Wu, J. et al. Electronic nematicity in Sr_2RuO_4 . *Proc. Natl Acad. Sci. USA* **117**, 10654–10659 (2020).
- Ando, Y., Segawa, K., Komiya, S. & Lavrov, A. N. Electrical resistivity anisotropy from self-organized one dimensionality in hightemperature superconductors. *Phys. Rev. Lett.* 88, 137005 (2002).
- Hinkov, V. et al. Electronic liquid crystal state in the high-temperature superconductor YBa₂Cu₃O_{6.45}. Science 319, 597–600 (2008).
- Jiang, Y. et al. Charge order and broken rotational symmetry in magic-angle twisted bilayer graphene. Nature 573, 91–95 (2019).
- 9. Choi, Y. et al. Electronic correlations in twisted bilayer graphene near the magic angle. *Nat. Phys.* **15**, 1174–1180 (2019).
- Kerelsky, A. et al. Maximized electron interactions at the magic angle in twisted bilayer graphene. Nature 572, 95–100 (2019).
- Cao, Y. et al. Nematicity and competing orders in superconducting magic-angle graphene. Science 372, 264–271 (2021).
- 12. Rubio-Verdú, C. et al. Moiré nematic phase in twisted double bilayer graphene. *Nat. Phys.* **18**, 196–202 (2022).
- Zhang, N. J., Watanabe, K., Taniguchi, T., Vafek, O. & Li, J. I. A. Electronic anisotropy in magic-angle twisted trilayer graphene. Preprint at https://arxiv.org/abs/2211.01352 (2022).
- 14. Lin, J.-X. et al. Spontaneous momentum polarization and diodicity in Bernal bilayer graphene. Preprint at https://arxiv.org/abs/2302.04261 (2023).
- Dong, Z., Davydova, M., Ogunnaike, O. & Levitov, L. Isospin- and momentum-polarized orders in bilayer graphene. *Phys. Rev. B* 107, 075108 (2023).
- 16. Jung, J., Polini, M. & MacDonald, A. H. Persistent current states in bilayer graphene. *Phys. Rev. B* **91**, 155423 (2015).
- Huang, C. et al. Spin and orbital metallic magnetism in rhombohedral trilayer graphene. Phys. Rev. B 107, L121405 (2023).
- Vafek, O. Anisotropic resistivity tensor from disk geometry magnetoconductance. Phys. Rev. Applied 20, 064008 (2023).
- 19. Zondiner, U. et al. Cascade of phase transitions and Dirac revivals in magic-angle graphene. *Nature* **582**, 203–208 (2020).
- 20. Park, J. M., Cao, Y., Watanabe, K., Taniguchi, T. & Jarillo-Herrero, P. Flavour Hund's coupling, Chern gaps and charge diffusivity in moiré graphene. *Nature* **592**, 43–48 (2021).
- 21. Xie, M. & MacDonald, A. H. Weak-field Hall resistivity and spin-valley flavor symmetry breaking in magic-angle twisted bilayer graphene. *Phys. Rev. Lett.* **127**, 196401 (2021).
- Kang, J., Bernevig, B. A. & Vafek, O. Cascades between light and heavy fermions in the normal state of magic-angle twisted bilayer graphene. *Phys. Rev. Lett.* 127, 266402 (2021).
- Liu, X., Zhang, N., Watanabe, K., Taniguchi, T. & Li, J. Coulomb screening and thermodynamic measurements in magic-angle twisted trilayer graphene. *Nat. Phys.* 18, 522–527 (2022).
- Lin, J.-X. et al. Spin-orbit-driven ferromagnetism at half moiré filling in magic-angle twisted bilayer graphene. Science 375, 437–441 (2022).

- 25. Ma, Q. et al. Observation of the nonlinear Hall effect under time-reversal-symmetric conditions. *Nature* **565**, 337–342 (2019).
- 26. Kang, K., Li, T., Sohn, E., Shan, J. & Mak, K. F. Nonlinear anomalous Hall effect in few-layer WTe₂. *Nat. Mater.* **18**, 324–328 (2019).
- He, P. et al. Graphene moiré superlattices with giant quantum nonlinearity of chiral Bloch electrons. *Nat. Nanotechnol.* 17, 378–383 (2022).
- Sinha, S. et al. Berry curvature dipole senses topological transition in a moiré superlattice. Nat. Phys. 18, 765–770 (2022).
- Khalaf, E., Kruchkov, A. J., Tarnopolsky, G. & Vishwanath, A. Magic angle hierarchy in twisted graphene multilayers. *Phys. Rev. B* 100, 085109 (2019).
- Hao, Z. et al. Electric field-tunable superconductivity in alternating-twist magic-angle trilayer graphene. Science 371, 1133–1138 (2021).
- 31. Novoselov, K. S. et al. Electric field effect in atomically thin carbon films. Science **306**, 666–669 (2004).
- 32. Novoselov, K. S. et al. Two-dimensional gas of massless Dirac fermions in graphene. *Nature* **438**, 197–200 (2005).
- 33. Geim, A. K. & Grigorieva, I. V. Van der Waals heterostructures. Nature **499**, 419–425 (2013).
- 34. Novoselov, K., Mishchenko, A., Carvalho, A. & Neto, A. C. 2D materials and van der Waals heterostructures. *Science* **353**, aac9439 (2016).
- 35. Ajayan, P., Kim, P. & Banerjee, K. Two-dimensional van der Waals materials. *Phys. Today* **69**, 38–44 (2016).
- 36. Sharpe, A. L. et al. Emergent ferromagnetism near three-quarters filling in twisted bilayer graphene. Science **365**, 605–608 (2019).
- 37. Serlin, M. et al. Intrinsic quantized anomalous Hall effect in a moiré heterostructure. Science **367**, 900–903 (2020).
- Chen, S. et al. Electrically tunable correlated and topological states in twisted monolayer-bilayer graphene. *Nat. Phys.* 17, 374–380 (2021).
- 39. Polshyn, H. et al. Electrical switching of magnetic order in an orbital Chern insulator. *Nature* **588**, 66–70 (2020).
- Cheung, P., Bao, Z.-Q. & Zhang, F. Flavor symmetry and ferroelectric nematics in transition metal dichalcogenides. Preprint at https://arxiv.org/abs/1805.06493 (2018).
- 41. Lin, J.-X. et al. Zero-field superconducting diode effect in twisted trilayer graphene. *Nat. Phys.* **18**, 1221–1227 (2022).
- 42. Scammell, H. D., Li, J. & Scheurer, M. S. Theory of zero-field superconducting diode effect in twisted trilayer graphene. *2D Mater.* **9**, 025027 (2022).
- 43. Benyamini, A. et al. Fragility of the dissipationless state in clean two-dimensional superconductors. *Nat. Phys.* **15**, 947–953 (2019).

Publisher's note Springer Nature remains neutral with regard to jurisdictional claims in published maps and institutional affiliations.

Springer Nature or its licensor (e.g. a society or other partner) holds exclusive rights to this article under a publishing agreement with the author(s) or other rightsholder(s); author self-archiving of the accepted manuscript version of this article is solely governed by the terms of such publishing agreement and applicable law.

@ The Author(s), under exclusive licence to Springer Nature Limited 2024

Methods

Hysteresis in the mirror-axis orientation

Apart from the thermal cycle, hysteretic rotation in the mirror axis can also be induced by a large current bias.

Extended Data Fig. 2 demonstrates the current-induced tunability in the angular dependence of non-reciprocity. Extended Data Fig. 2a plots the angular dependence of $V_\perp^{2\omega}$ measured at the same carrier density with different current biases. The angular dependence behaves like a cosine function with a period of 2π at a low current bias. It changes to a linear combination of $\cos\phi$ and $\cos3\phi$ as the current bias is increased to I > 200 nA. At I = 400 nA, the angular dependence becomes largely three-fold symmetric, although the quality of angular fit becomes poorer at this large current.

The current-induced change in the angular dependence of non-reciprocity can be hysteretic, that is, the angular dependence of non-reciprocity, measured with a small current bias, is different before and after a large current bias. Extended Data Fig. 2b shows this hysteretic behaviour. Before (after) applying a large current bias at 1 μ A, the angular dependence measured at $\nu = -2.2$ is highlighted by the orange (blue) box in this figure. In both cases, the angular dependence is a linear combination of $\cos\phi$ and $\cos3\phi$. However, the mirror axis (Extended Data Fig. 2b, green solid lines) exhibits a prominent rotation before and after the current bias.

The hysteretic rotation gives rise to a hysteresis loop in the second-harmonic nonlinear response $R_{\perp}^{2\omega}$ (Extended Data Fig. 2c), which is defined as $V_{\perp}^{2\omega}/I$. The insets in Extended Data Fig. 2c show the schematic of the angular dependence measured before and after sweeping the current up and down.

Furthermore, we note that current-induced hysteresis usually occurs at a large current bias. Extended Data Fig. 3 shows the angular dependence of non-reciprocity η_{\parallel} measured with different d.c. current biases. Up to I=100 nA, the angular dependence of non-reciprocity, along with its associated mirror-axis orientation, remains the same. As such, the angular dependence reported in this work is mostly carried out at $I \le 100$ nA, unless otherwise specified.

Non-reciprocity and nonlinearity

Transport non-reciprocity η can be extracted from the I-V curve measured with a d.c. current bias. As shown in Extended Data Fig. 4a, the I-V curve deviates from the linear response (black dashed line) at a large current bias. As a result of the deviation, longitudinal resistance R_{\parallel} , defined as $R_{\parallel} = V_{\parallel}/I$, is larger at the positive current bias compared with the negative bias (Extended Data Fig. 4a, red circles). Subtracting the linear component reveals the non-reciprocal response $\Delta V_{\parallel} - R_0 I_{\rm d.c.}$, where R_0 denotes the slope of the I-V curve at $I_{\rm d.c.} = 0$. The non-reciprocal component is shown to have a quadratic current dependence, namely, $\eta \approx I^2$ (Extended Data Fig. 4b (black solid line) is a quadratic fit to the data).

Given the quadratic current dependence in η , non-reciprocity is proportional to $\sin^2 \omega t$ in the presence of an a.c. current bias with frequency ω , which has the same frequency modulation as $\sin(2\omega t)$. As such, η is equivalent to the nonlinear transport response measured at the second-harmonic frequency of an a.c. current bias.

Extended Data Fig. 5 compares the angular dependence of transport non-reciprocity with the nonlinear response at the second-harmonic frequency. The azimuth angle ϕ defines the direction of current flow across the sunflower-shaped sample. Different ϕ values are realized using the measurement configurations shown in Extended Data Fig. 1.

Extended Data Fig. 5b,d plots the angular dependence of η , which is extracted from the d.c. transport I-V curves with current flowing in different azimuth directions. The value of η along ϕ is defined as the difference in R between the current flowing in the azimuth direction of ϕ and $\phi + \pi$:

$$\eta(\phi) = R(\phi) - R(\phi + \pi). \tag{1}$$

Here R is the transport response at a fixed d.c. current value of $I_{\rm d.c.} = 100$ nA. By definition, η displays a sign reversal between the forward- and reverse-current bias.

Extended Data Fig. 5a,c plots the angular dependence of the second-harmonic nonlinear transport response $V^{2\omega}$, which is measured at the same band fillings as those shown in Extended Data Fig. 5b,d. The value of $V^{2\omega}$ along ϕ is simply defined as the voltage response at the second-harmonic frequency as an a.c. current is biased along the azimuth direction of ϕ . On the basis of this comparison, we make a few important observations: (1) the angular dependence of n shows excellent agreement with that of the second-harmonic nonlinear response $V^{2\omega}$; (2) the angular dependence can be captured by a linear combination of one-fold- and three-fold-symmetric components; (3) the one-fold-symmetric component of angular dependence is aligned along the corner of the Brillouin zone. The azimuth directions of all the six corners correspond to the plateau values shown in Fig. 3c. Combined, the angular dependence of transport non-reciprocity and second-harmonic nonlinear response offer further confirmation for the exchange-driven instability in valley and momentum space.

Mean-square error in angular fit

Extended Data Fig. 6 demonstrates the procedure for determining the best angular fit for transport non-reciprocity. In general, the best angular fit is obtained by minimizing the RRMSE, which is defined as

RRMSE =
$$\frac{\sqrt{\frac{1}{N}\sum_{i}(V_{i}-V_{i}^{0})^{2}}}{\sqrt{\sum_{i}(V_{i})^{2}}}$$
, (2)

where V_i is the ith point of the measurement results and V_i^0 is the value of the best fit at the corresponding azimuth direction. Also, N denotes the number of points. Furthermore, N=32 for the angular fit for longitudinal and transverse responses, since there are 16 angles for each transport channel. Extended Data Fig. 6b,d shows the evolution of the RRMSE as one of the fit parameters deviates from the parameter of the best angular fit, whereas the other two fit parameters are fixed at the value of the best fit. According to equation (1), the fit parameters V_1, V_3 and β create a three-dimensional phase space for identifying the best angular fit. For angular dependence (Extended Data Fig. 6a,c), RRMSE is around 5% for the best fit. This indicates that the angular dependence of non-reciprocity is well captured by equation (1).

Extended Data Fig. 7 examines the best fit for the angular dependence at ν = 2.15, where the best fit features a strong three-fold-symmetric component. The RRMSE of the best fit is around 8%. Although slightly larger compared with Extended Data Fig. 6, an RRMSE below 10% is considered agood angular fit. That a predominantly three-fold-symmetric behaviour has slightly higher error is understandable, since the angular oscillation is approaching the resolution of the sunflower geometry. We note that the right panel of Extended Data Fig. 7b exhibits two extra local minima in RRMSE, which are located $2\pi/3$ away from the optimal value of β . These two local minima provide a strong indication for the three-fold-symmetric component in the angular dependence of non-reciprocity.

Potential impact of moiré disorder, sample uniformity and ballistic transport

Extended Data Fig. 8a plots the angular dependence of the linear transport response, namely, R_{\parallel} and R_{\perp} . The angular dependence is in excellent agreement with the expected behaviour of orthorhombic anisotropy (Fig. 1d). The angular oscillation points towards two orthogonal mirror axes. The sample exhibits different conductivities as current flows along each mirror axis. The angular dependence shown in Extended Data Fig. 8a can be captured by a conductivity matrix. According to another work 18, the knowledge of the conductivity matrix allows us to compute the potential distribution across the entire sample, as long as electrons diffusively move through the sample, that is, electron transport is non-ballistic.

The geometry of the sunflower sample features eight electrical contacts (petals) attached to the circumference of a circular sample channel. The geometry allows more than 400 independent measurement configurations: picking any two contacts as the source and drain, a voltage measurement can be performed across any two of the remaining contacts. Although 400 configurations appear redundant, they allow us to fully map the potential distribution across the circumference of the sample. By fitting these measurements with a single conductivity matrix using the sunflower model, we can gain insights into the uniformity of transport response across the sample.

Extended Data Fig. 8b plots the results from a subset of all the independent measurement configurations. Here the red circles denote the measured value, and the insets show the schematic of each measurement configuration. Also, the horizontal grey stripe is the expected value predicted by the sunflower model based on a single conductivity matrix 18 . The width of the grey stripe arises from the non-zero width of each electrical contact, which gives rise to a range of possible electrical potentials.

Noticeably, the measurement configurations from the same row are associated with an in-plane rotation. In the absence of electronic anisotropy, we anticipate the same measurement results from different configurations of the same row. That is, variations in the transport response across each row directly arises from the presence of electronic anisotropy. Different measurement configurations probe slightly different parts of the sample. For example, configurations in the fourth row from the top probe the transport response close to the circumference of the sample. Results from all the measurement configurations are reasonably captured by a single conductivity matrix. The RRMSE of this fit is around 0.017, which points to an excellent agreement between the measurement and the model. The excellent fit provides a strong indication that the transport response is uniform across the entire sample.

As a by-product, the fit shown in Extended Data Fig. 8b suggests that electron transport through the sample is non-ballistic.

Extended Data Fig. 8c displays the angular dependence of transport non-reciprocity measured at the same band filling. Here the green solid lines mark the orientation of the mirror axis. At this band filling, the mirror axis extracted from non-reciprocity is close to being aligned with the principle axis of the linear component of the transport response. In the 'Nematicity and momentum polarization' section in the Supplementary Information, we offer a more detailed discussion regarding the relationship between the mirror axis of non-reciprocity and the principle axis of linear transport.

Data availability

Data presented in this work are attached. Source data are provided with this paper. Additional data are available from the corresponding author upon request.

Acknowledgements

J.I.A.L. wishes to thank O. Vafek and D. Feldman for stimulating discussions. L.F. thanks the organizers of the workshop 'Superconducting diode effects' on Virtual Science Forum, which ignited the collaboration. This material is based on the work supported by the Air Force Office of Scientific Research under award no. FA9550-23-1-0482. N.J.Z. acknowledges support from the Jun-Qi fellowship and the Air Force Office of Scientific Research. J.-X.L. and J.I.A.L. acknowledge funding from NSF DMR-2143384. Device fabrication was performed in the Institute for Molecular and Nanoscale Innovation at Brown University. D.V.C. acknowledges financial support from the National High Magnetic Field Laboratory through a Dirac Fellowship, which is funded by the National Science Foundation (grant no. DMR-1644779) and the State of Florida. K.W. and T.T. acknowledge support from the Elemental Strategy Initiative conducted by the MEXT, Japan (grant no. JPMXP0112101001), and JSPS KAKENHI (grant nos. 19H05790, 20H00354 and 21H05233). The work at the Massachusetts Institute of Technology was supported by a Simons Investigator Award from the Simons Foundation.

Author contributions

N.J.Z. and J.I.A.L. conceived the project. N.J.Z. and Y.W. fabricated the device. N.J.Z., J.-X.L. and Y.W. performed the measurement. D.V.C. and L.F. provided theoretical inputs. K.W. and T.T. provided the material. N.J.Z., L.F. and J.I.A.L. wrote the manuscript.

Competing interests

The authors declare no competing interests.

Additional information

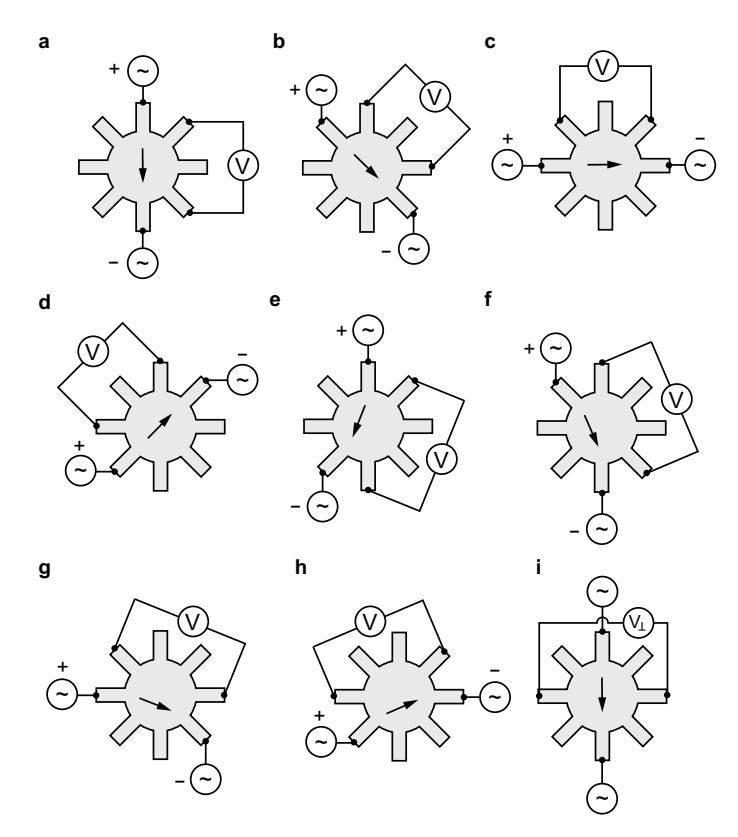
Extended data is available for this paper at https://doi.org/10.1038/s41563-024-01809-z.

Supplementary information The online version contains supplementary material available at https://doi.org/10.1038/s41563-024-01809-z.

Correspondence and requests for materials should be addressed to J. I. A. Li.

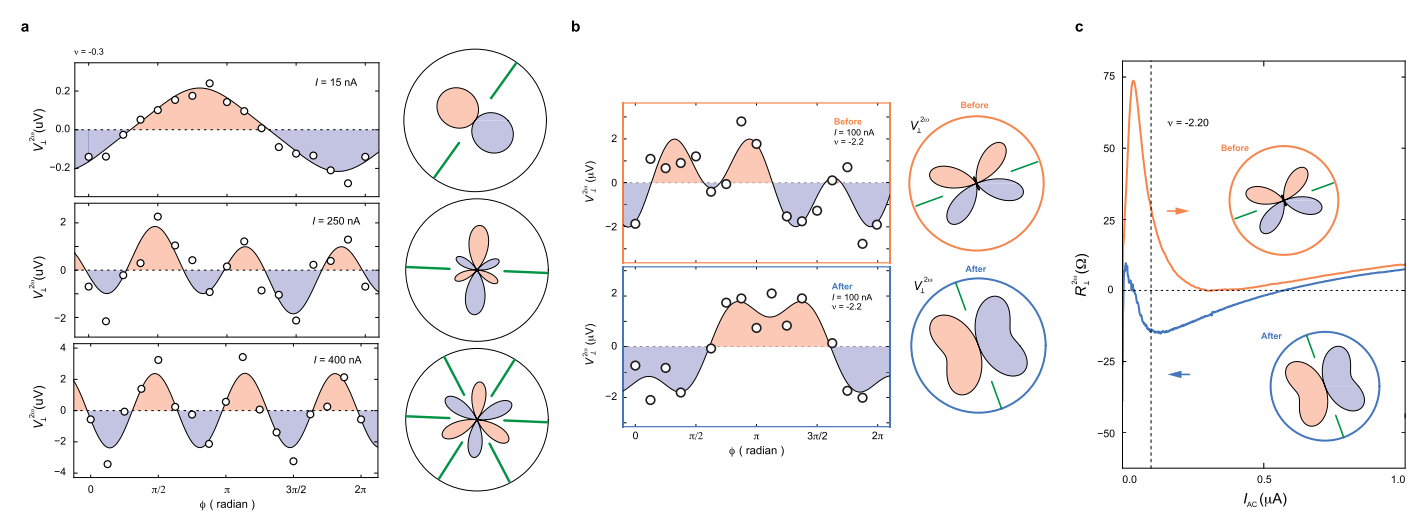
Peer review information *Nature Materials* thanks the anonymous reviewers for their contribution to the peer review of this work.

Reprints and permissions information is available at www.nature.com/reprints.



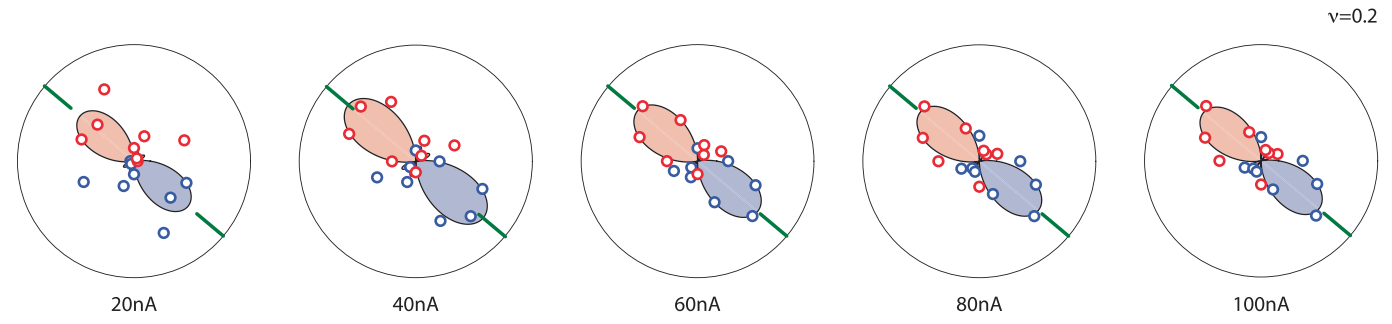
Extended Data Fig. 1| **Measurement setup.** (a-h) Schematic diagram showing the measurement configuration with current flowing is different azimuth directions ϕ across the 'sunflower' sample. For each ϕ , the longitudinal transport response is defined as the voltage difference across two contacts (each contact resembles a petal of the 'sunflower'), which are aligned parallel to the direction of current flow. Panels (a) to (h) show measurement configurations for 8 azimuth directions. Along the same vein, the transverse response is measured across two contacts aligned perpendicular to the current flow direction, as shown in panel

(i). We use $V_{\parallel}(V_{\perp})$ to denote the voltage difference across two contacts that are parallel (perpendicular) to the current flow direction (Fig. 1a). Instead of applying current bias at the source contact and short to ground at the drain contact, we apply a positive current bias to the source contact, and a negative bias to the drain contact. This ensures that the center of the sample remains at zero electric potential, thus suppressing the potential influence of capacitive coupling and thermal-electric effects associated with the contact resistance.

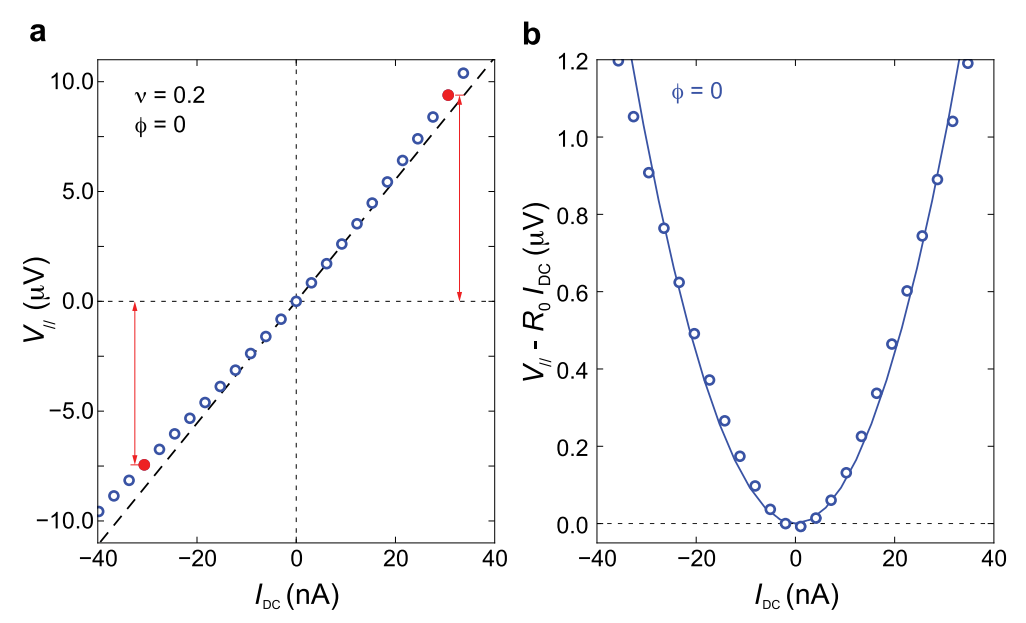


Extended Data Fig. 2 | **Current-induced Hysteresis in nonreciprocity.** (a) The angular dependence of nonreciprocity measured at the same moiré band filling v=-0.3 and different current bias. At a small current bias, the angular dependence is best described by a one-fold symmetric cosine function. With increasing current, the angular dependence starts to evolves into a mixture between one- and three-fold at I>200 nA. Further increasing the current bias gives rise to angular dependence at I=400 nA that is best captured by $\cos 3\phi$. (b) The angular dependence of nonreciprocity at v=-2.2 before (top panel) and

after (bottom panel) the application of a large current bias. The large current bias induces a hysteretic rotation in the underlying mirror axis, which is marked by the green solid line in the polar coordinate plots. (c) $R_{\perp}^{2\omega}$, defined as $V_{\perp}^{2\omega}/I$, as a function of current bias. As the current bias is swept back and forth, $R_{\perp}^{2\omega}$ exhibits a hysteresis loop. The angular dependence of $V_{\perp}^{2\omega}$ in panel (b) is measured before and after this hysteresis loop at a fixed current bias of I=100 nA. Inset shows the schematic angular dependence for the data shown in panel (b).

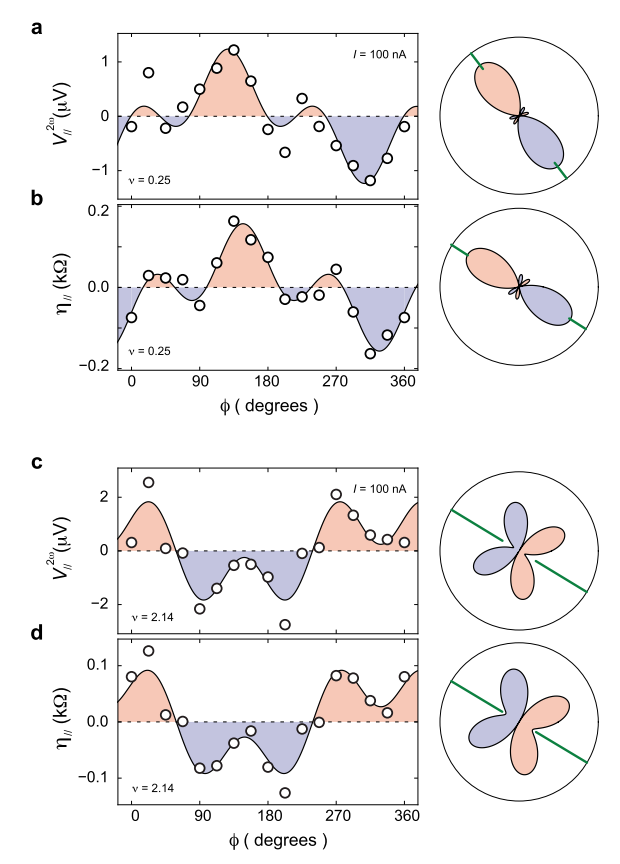


Extended Data Fig. 3 | Angle dependence of η_{\parallel} measured at different DC current bias. Polar-coordinate plot of the angle dependence of η_{\parallel} , measured at B=0, T=20 mK and $\nu=0.2$. With increasing DC current bias, a similar angular dependence that is predominantly one-fold symmetric is observed up to $I_{DC}=100$ nA, all pointing towards around 140°.



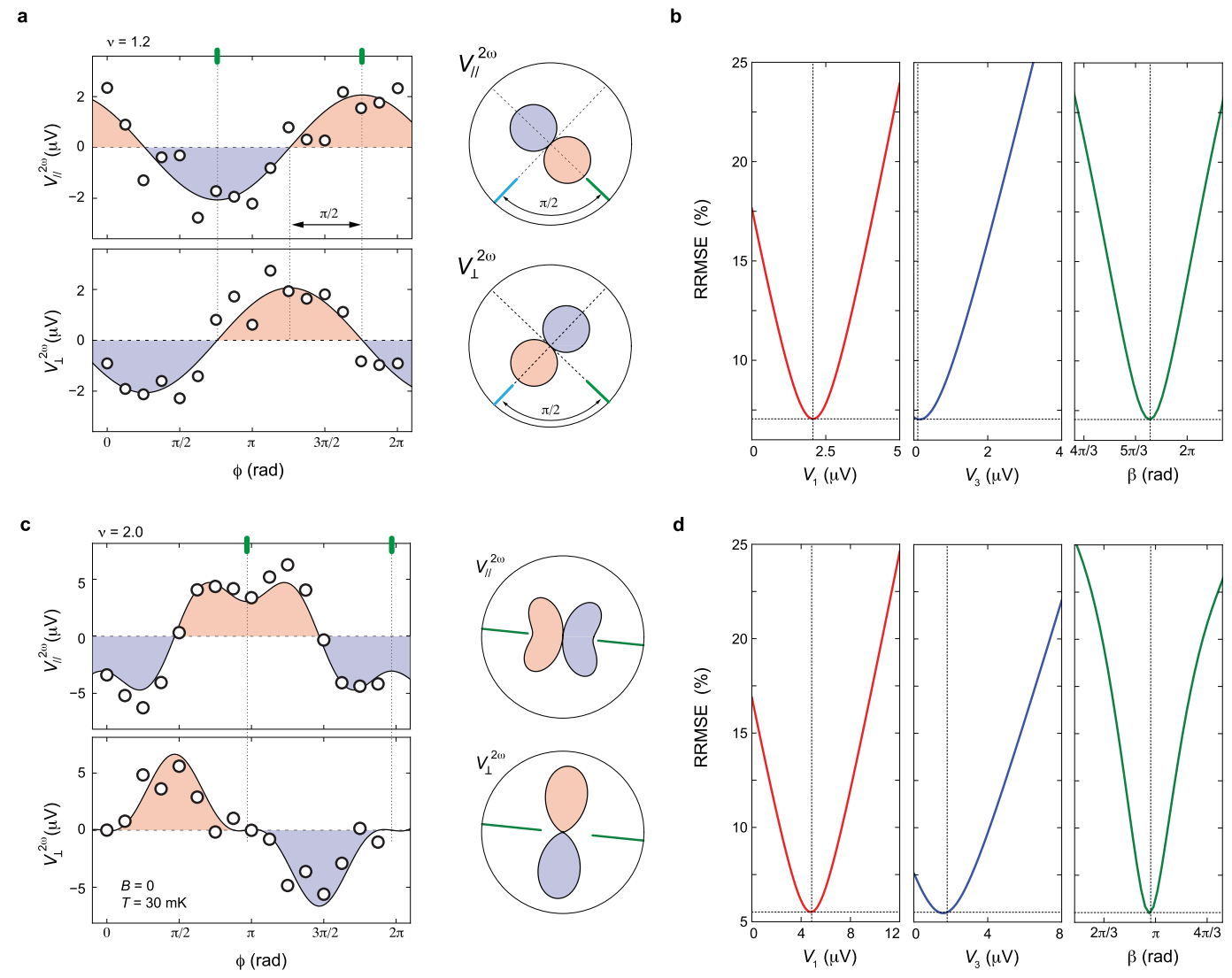
Extended Data Fig. 4 | **Nonreciprocity and nonlinearity.** (a) Current-voltage characteristic measured at $\nu=-0.3$ with DC current flowing along azimuth angle of $\phi=0$ °. The black dashed line is a linear fit to the portion of the IV curve near zero current bias. (b) The nonreciprocal component of the IV curve, which

is extracted by subtracting the ohmic component of the transport response, $\eta/2 = V_{\parallel} - I_{DC}R_0$. R_0 denotes the slope of the IV curve at $I_{DC} = 0$ The solid line is a quadratic fit to the current dependence of $\eta/2$.



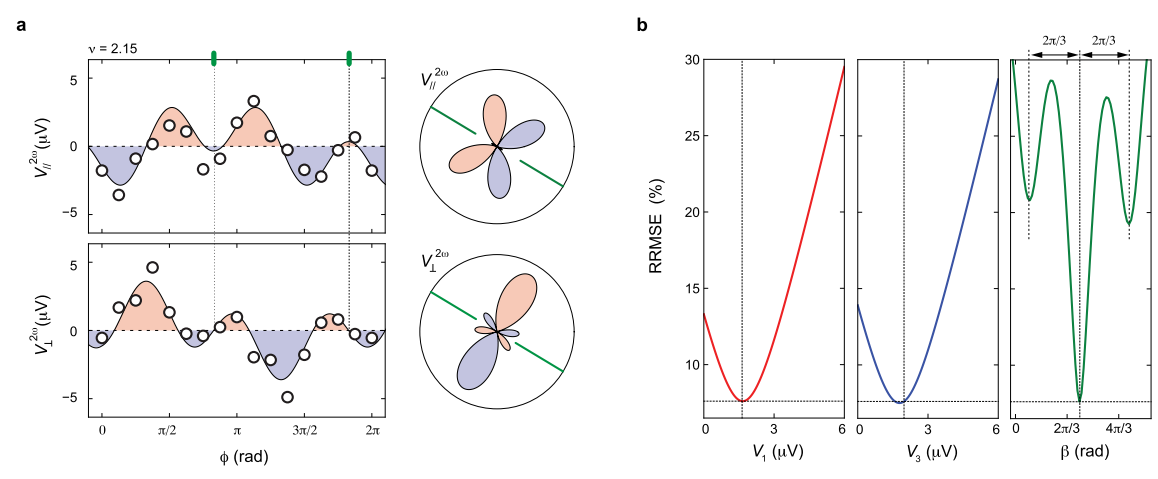
Extended Data Fig. 5 | Second-harmonic nonlinear response and transport nonreciprocity. Angle dependence measurement of (a) $V_{\parallel}^{2\omega}$ and (b) η_{\parallel} at ν = 0.25 and (c) $V_{\parallel}^{2\omega}$ and (d) η_{R} at ν = 2.14. The remarkable match in the angle dependence

between $V_{\parallel}^{2\omega}$ and (b) η_{\parallel} at different densities illustrates their correspondence relation. $V_{\parallel}^{2\omega}$ are measured at I_{AC} = 100 nA, η_R are measured at I_{DC} = 100 nA. All measurements are performed at B = 0 and T = 20 mK.

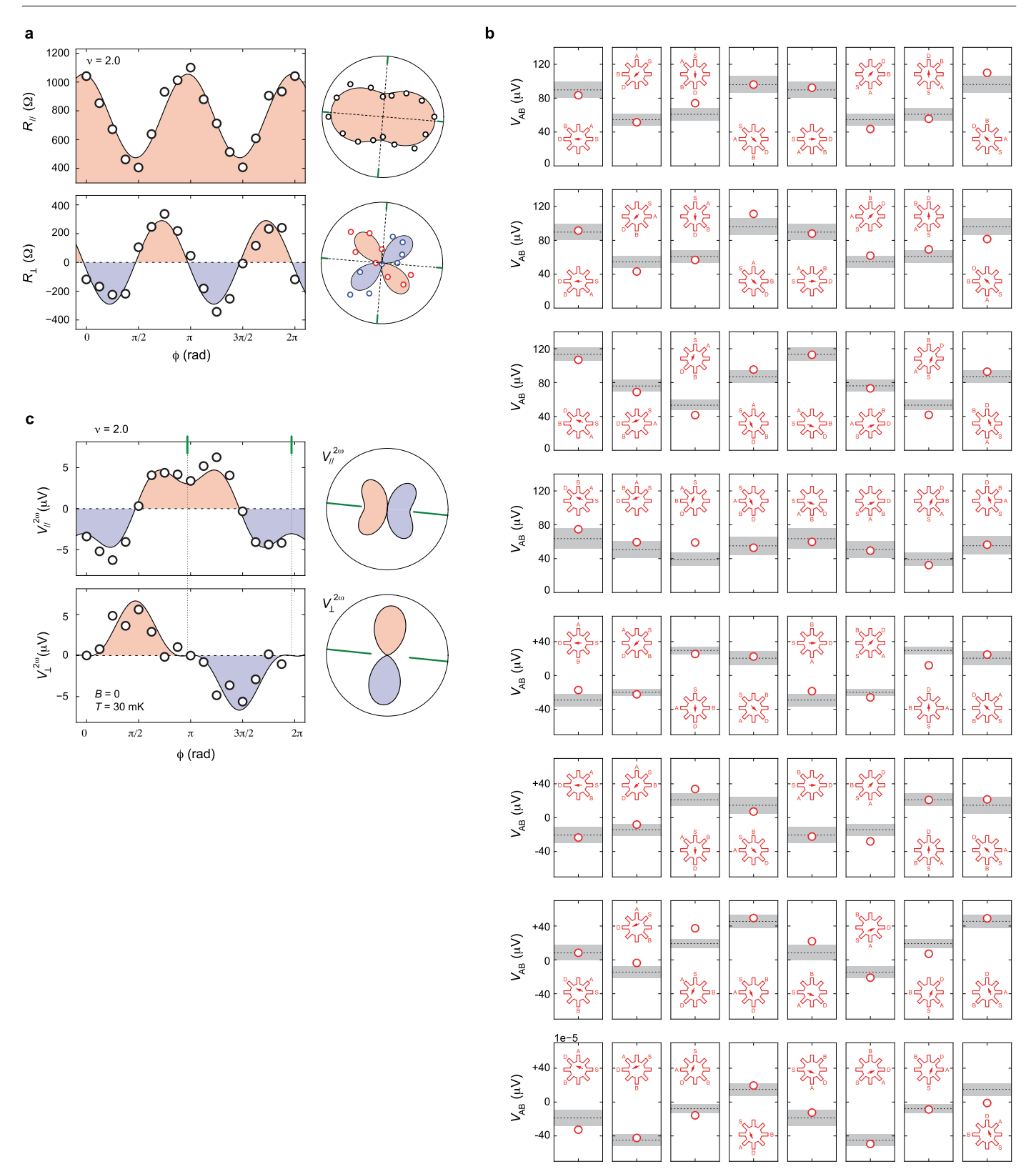


Extended Data Fig. 6 | **Relative Root Mean Squared Error in the angular fit** with large V_1 . (a) The angular dependence of nonreciprocity measured at v=1.2. (b) Relative root-mean-squared error (RRMSE), defined according to Eq. M2, as a function of V_1 (left panel), V_3 (middle panel), and β (right panel). (c) The angular

dependence of nonreciprocity measured at v = 2.0. (d) Relative root-mean-squared error (RRMSE), defined according to Eq. M2, as a function of V_1 (left panel), V_3 (middle panel), and β (right panel).

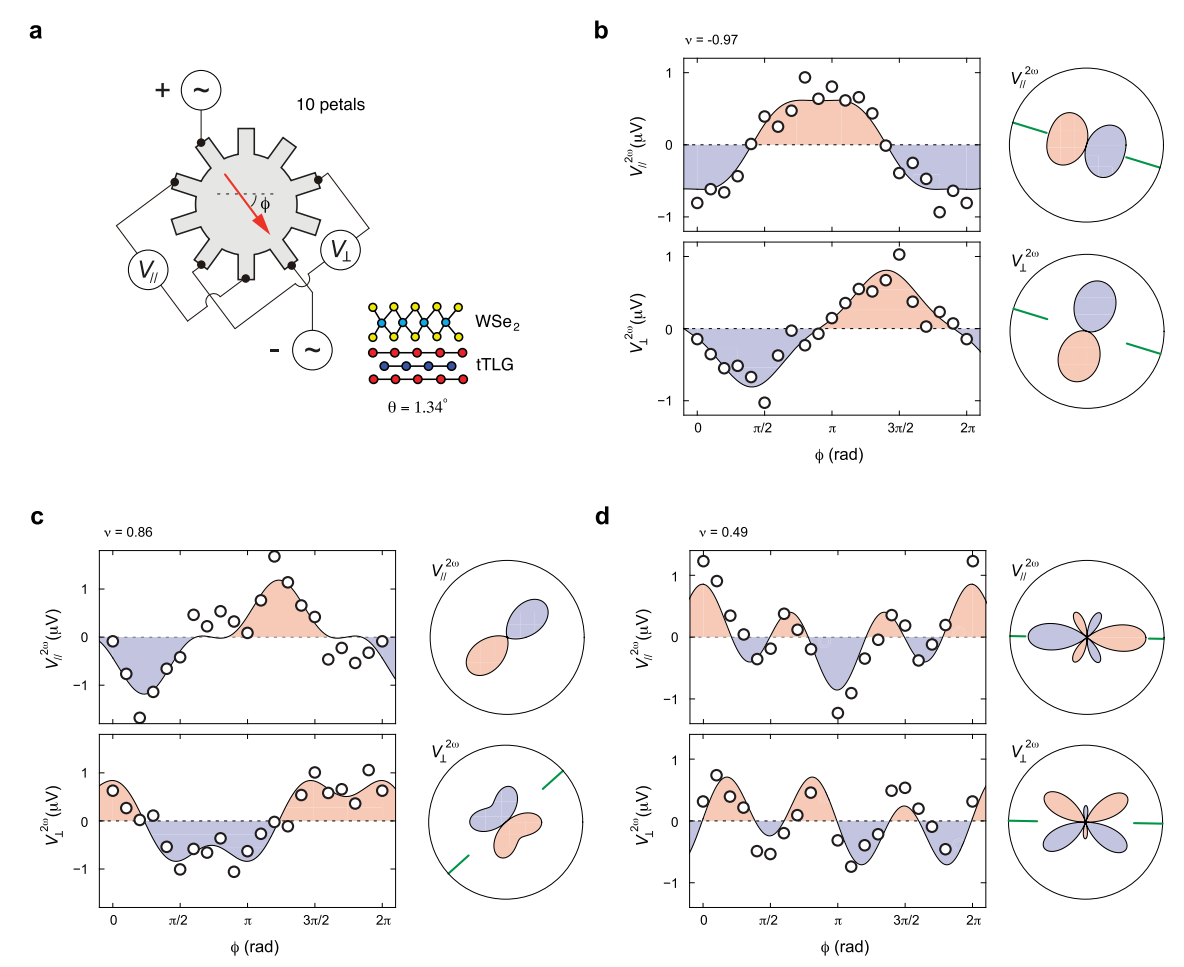


Extended Data Fig. 7 | **Relative Root Mean Squared Error in the angular fit with large** V_3 **.** (a) The angular dependence of nonreciprocity measured at v = 2.15. (b) Relative root-mean-squared error (RRMSE), defined according to Eq. M2, as a function of V_1 (left panel), V_3 (middle panel), and β (right panel).



Extended Data Fig. 8 | **The 'sunflower' model beyond angular fit.** (a) The angular dependence of longitudinal and transverse resistance, R_{\parallel} and R_{\perp} , measured at ν = 2. (b) Measurements from different 'sunflower' configurations compared to the expected value extracted from a single conductivity matrix^{13,18}.

The RRMSE of the fit is 1.74%. (c) The angular dependence of longitudinal and transverse second-harmonic nonlinear transport response, $V^{2\omega}_{\parallel}$ and $V^{2\omega}_{\perp}$, measured with an AC current of 100 nA at ν = 2.



Extended Data Fig. 9 | **Angle-resolved nonreciprocity measurement with higher angular resolution.** (a) Schematic diagram of the 'sunflower'-shaped sample with 10 petals. The increased number of electrical contacts enables higher angular resolution in the nonreciprocity measurement. (b-d) Angle-resolved nonreciprocity measured at different moiré band filling of the tTLG sample, which has a twist angle of θ = 1.34°. The best angular fit for the angular dependence (black solid line) is captured by Eq. 1, which is extracted by minimizing the RRMSE of nonreciprocity from both longitudinal and transverse channels. With increased angular resolution, the best fit to the angular

dependence of nonreciprocity in panel (b) features RRMSE of 0.3%, while other angular dependence shows RRMSE of less than 2%. Beyond the one-fold and three-fold components, the next lowest order angular component is described by $\cos(5\phi)$ and $\sin(5\phi)$. While an oscillatory period of 72° is well within the measurement resolution, such a component is not observed in our measurement. This is a strong indication that the angular components with N>3 has small oscillatory amplitude. All measurement performed at T=20 mK, B=0, and $I_{AC}=50$ nA.